



**HAL**  
open science

## Toward hybrid CAA with ground effects

Marc Jacob, D. Dragna, A. Cahuzac, J. Boudet, Ph. Blanc-Benon

► **To cite this version:**

Marc Jacob, D. Dragna, A. Cahuzac, J. Boudet, Ph. Blanc-Benon. Toward hybrid CAA with ground effects. *International Journal of Aeroacoustics*, 2014, 13 (3-4), pp.235-260. 10.1260/1475-472X.13.3-4.235 . hal-01136620

**HAL Id: hal-01136620**

**<https://hal.science/hal-01136620>**

Submitted on 11 Apr 2016

**HAL** is a multi-disciplinary open access archive for the deposit and dissemination of scientific research documents, whether they are published or not. The documents may come from teaching and research institutions in France or abroad, or from public or private research centers.

L'archive ouverte pluridisciplinaire **HAL**, est destinée au dépôt et à la diffusion de documents scientifiques de niveau recherche, publiés ou non, émanant des établissements d'enseignement et de recherche français ou étrangers, des laboratoires publics ou privés.

## ***Toward hybrid CAA with ground effects***

**M. C. Jacob, D. Dragna, A. Cahuzac, J. Boudet and Ph. Blanc-Benon**

*Centre Acoustique du LMFA, UMR CNRS 5509 – Ecole Centrale de Lyon –*

*Université Claude-Bernard Lyon I, F-69134 Ecully Cedex*

*marc.jacob@ec-lyon.fr, didier.dragna@ec-lyon.fr, adrien.cahuzac@ec-lyon.fr,*

*jerome.boudet@ec-lyon.fr, philippe.blanc-benon@ec-lyon.fr*

*Received May 1, 2013; Revised April 21, 2014; Accepted May 1, 2014*

### **ABSTRACT**

CAA based on the Linearised Euler Equations (LEE) is applied to propagate aerodynamic sound over an extended distance including ground effects. The LEE are coupled to data from an LES via an acoustic analogy to follow-up the sound from the source to the extended far field: the complete chain is illustrated on the sound generated by a cylinder in a  $M \sim 0.2$  and  $Re \sim 48000$  flow. A very good agreement is found in free field between the approach based on the Ffowcs-Williams & Hawkings (FWH) analogy only and the combined FWH-LEE approach. The ability of the combined approach to handle complex boundary conditions is illustrated on the same data set with a rigid and a grassy ground.

### **NOMENCLATURE**

$A_k$ :	coefficient associated to $k$ -th pole of the rational approximation of $\hat{Z}(\omega)$
$c_0$ :	sound speed in fluid at rest
$c_{eq}$ :	equivalent sound speed taking into account the mean flow velocity $V_0$
$\overline{C_D}$ :	mean drag coefficient
$C_D'$ :	rms-value of drag fluctuations
$C_f$ :	friction coefficient
$C_L'$ :	rms-value of lift fluctuations
$c_p$ :	specific heat
$C_p$ :	pressure coefficient
$C_p'$ :	rms value of pressure coefficient
$C_S$ :	Smagorinsky constant
$ds$ :	surface element
$D$ :	cylinder diameter
$e_t$ :	total specific energy
$f$ :	frequency
$f_0$ :	shedding frequency

- $2f_0, 2mf_0$ : 1<sup>st</sup> and  $(2m-1)$ <sup>th</sup> harmonic (uneven)  
 $3f_0, ((2m+1)f_0)$ : 2<sup>nd</sup> and  $(2m)$ <sup>th</sup> harmonic (even)  
**F**: unsteady external force per unit volume in LEE  
 $g = 0$ : equation of control surface in the FWH analogy  
**H**: Heaviside function  
*i, j, k, m*: integers  
**L**: cylinder length (span) in the computation  
 $L_{exp}$ : cylinder length in the experiment  
 $l_r$ : length of recirculation bubble in the near cylinder wake  
 $L_i$ : unsteady loading on the FWH control surface  $g = 0$   
**M**: Mach number  
 $M_r = \mathbf{M} \cdot \mathbf{r} = \frac{M_i r_i}{r}$ : Mach number in local observer direction  
**n, n<sub>i</sub>**: exterior normal: vector and *i*-th component  
**N**: number of poles of  $\hat{Z}(\omega)$   
**O**: origin of coordinate system, located on the cylinder centre at mid-span  
*p*: pressure  
 $p_0$ : unperturbed air pressure  
 $p'$ : acoustic pressure perturbation  
 $\hat{p}(\omega)$ : Fourier transform of the acoustic pressure  $p'$  at the ground  
 $Pr_{sgs} = \frac{\mu_{sgs} c_p}{\kappa}$ : subgrid-scale Prandtl number  
*q*: unsteady mass flow rate source per unit volume in LEE  
**Q**: unsteady mass flux through the FWH control surface  $g = 0$   
**r, r**: local source-to-observer position, vector and modulus  
 $r\Delta\theta_{max}^+$ : maximum azimuthal grid spacing at the wall in wall units  
**R**: distance from origin to observer (origin located at mid-span centre of cylinder section)  
**Re**: diameter-based Reynolds number  
 $S_{ij}$ : local strain rate tensor component  
**St**: Strouhal number (dimensionless frequency)  
*t, t'*: time  
 $u_p, v_i$ : instantaneous velocity component in *i*-th direction  
 $u_x$ : streamwise instantaneous velocity  
 $u_y$ : velocity fluctuation in cross-stream direction  
 $u_z$ : velocity fluctuation in spanwise (vertical) direction  
 $u_n, v_n$ : unsteady normal velocity components  
**v**: velocity fluctuation in LEE  
 $\hat{v}_n(\omega)$ : Fourier transform of the acoustic velocity normal to the ground  
**V**: wind speed  
 $V_0$ : incoming uniform flow velocity for cylinder flow, (also vehicle speed on Fig.1)  
 $\mathbf{V}_0$ : unperturbed velocity field – also  $V_0 = \|\mathbf{V}_0\|$  in cylinder flow

$\mathbf{x}, x_i$ :	observer position (vector, component) with respect to origin
$\mathbf{y}, y_i$ :	position (vector, $i$ -th component in generic coordinate system) with respect to origin
$(x, y, z)$ :	coordinate system for the cylinder: streamwise, cross-stream and spanwise directions respectively
$y_{ref}$ :	$y$ -position of the inlet boundary for the long-range computation
$Z(t), \hat{Z}(\omega)$ :	impedance in time and frequency domain respectively
$Z_\infty$ :	limit value of $\hat{Z}(\omega)$ as $\omega$ tends to infinity
$\Delta$ :	filter size
$\Delta r_{max}^+$ :	maximum radial grid spacing at the wall in wall units
$\Delta z_{max}^+$ :	maximum spanwise grid spacing at the wall in wall units
$\delta$ :	Dirac function
$\Delta t$ :	time step
$\theta$ :	observer angle in $(x, y)$ mid-span plane with respect to the cylinder centre and the upstream direction $(O, -x)$
$\theta_S$ :	angular position of separation point on cylinder
$\kappa$ :	thermal conductivity
$\lambda$ :	wavelength
$\lambda_k$ :	$k$ -th pole of the rational approximation of $\hat{Z}(\omega)$
$\mu$ :	molecular viscosity
$\mu_{sgs}$ :	subgrid-scale viscosity
$\rho$ :	air density
$\rho_0$ :	air density in medium at rest
$\sigma_{ij}$ :	deviator component of the double strain rate tensor: $i$ -th line, $j$ -th column
$\tau_{ij}$ :	viscous stress: $i$ -th line, $j$ -th column
$\tau_{ret}$ :	retarded time
$\varphi$ :	observer angle in $(y, z)$ plane (normal to flow direction) with respect to the cylinder centre and the cross-stream direction $(O, y)$
$\phi_k$ :	accumulator associated to the $k$ -th pole of the rational approximation of $\hat{Z}(\omega)$
$\omega$ :	angular frequency
$\overline{\dots}$ :	(overbar) filtered quantity
$\widetilde{\dots}$ :	(overtilde) Favre-filtered quantity (density weighted filter)
$\hat{\dots}$ :	Fourier transform
$\dots^{(m)}$ :	value at discretised time $m\Delta t$
$[\dots]_{ret}$ :	quantity in brackets is evaluated at retarded time $\tau_{ret}$

## ACRONYMS

BC: Boundary Condition	LES: Large-Eddy Simulation
CAA: Computational AeroAcoustics	PSD: Power Spectral Density
CFD: Computational Fluid Dynamics	RANS: Reynolds Averaged Navier Stokes (equations)
FWH: Ffowcs Williams Hawkins (analogy)	SISM: Shear-Improved Smagorinsky Model
HST: High Speed Train	TDBC: Time Domain Boundary Condition
LEE: Linearised Euler Equations	1D, 2D, 3D: one-, two-, three- dimensional

## 1. INTRODUCTION

### Background

Many aeroacoustic sources are located on or near the ground when they cause the strongest annoyance to neighbourhoods. This is clearly the case for high-speed ground transportation (*e.g.* High Speed Trains (HST) or planes at take off, landing and taxiing) where sources such as pantographs, bogies, wipers, airframe singularities or jet-engines radiate aerodynamic noise near the ground. In such applications the ground can generally not be approximated by a rigid plane since it is neither flat (see Figure 1) nor hard. The presence of ballast, grass etc. requires taking into account absorption and phase shift *via* an impedance model.

In classical approaches, propagation is computed in the frequency domain, typically with Boundary Element Methods and as a result, both impedance and ground geometry are easily modelled but air inhomogeneity and ambient flow conditions are difficult to include into these models. Therefore time-domain approaches appear to be more appropriate. In particular, when it comes to far field prediction with time-domain Computational AeroAcoustic (CAA) codes, the Linearised Euler Equations (LEE) based codes have shown to be an efficient tool if the ground impedance is suitably modelled. Such impedance models are available in the literature (*e.g.* Miki [1], Hamet and Bérengier [2]). Long range propagation predictions using LEE codes have been tested for academic sources in complex environments (non plane ground topography) in two- and three-dimensional domains: Cotté *et al.* [3] tested various ground impedances whereas Dragna *et al.* [4]-[6] took into account meteorological effects by introducing a vertical sound speed or wind speed gradient. More recently, their LEE code has been used to study the acoustic radiation of sources in motion above an impedance plane [7]. Although most examples in the railway applications are limited to an observer distance of 25 m (as certification points are 7.5 m and 25 m off-the train), the long-range

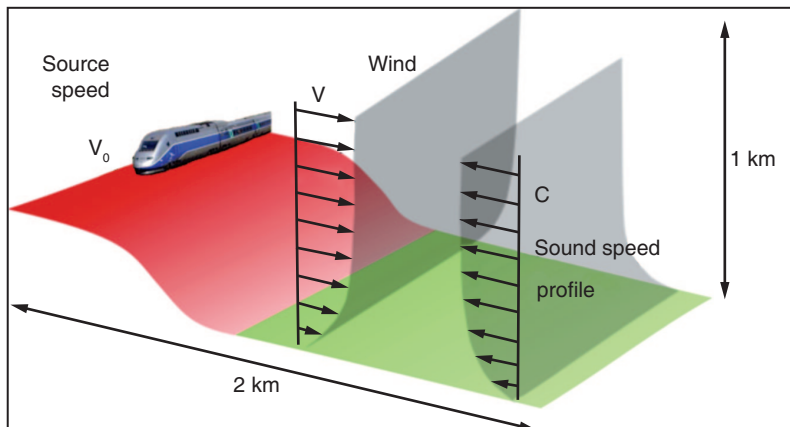


**Figure 1:** Sound propagation nearby a railway track.

propagation tool developed by these authors reaches about 500 m for a 1 kHz source on desktop computers. The reason for this moderate cost is that only the propagation of given sound waves is addressed but not the generation of the sound waves by the flow, and as a result the mesh size is based on the wavelength rather than on the length scale of the flow eddies. A similar tool has also been applied to very long-range and non-linear propagation of infrasound in the atmosphere by Marsden *et al.*[8]. Thus the LEE code is flexible and may be applied to many complex situations that make it particularly appealing for near ground propagation.

However, since the surroundings of the aerodynamic sources cannot be included in the CAA domain, the aeroacoustic sound generation has to be addressed by a separate tool. This could ideally be a high-order LES or hybrid RANS-LES computation that accurately resolves the unsteady flow and the acoustic waves up to the outer boundaries of a CFD domain surrounding the source region. In real life applications, the turbulent flow region is much larger than the source region due to the fact the vehicle dimensions are typically one or two orders of magnitude larger than the noisy components (*e.g.* pantograph for a train, landing gear or flap edges for a plane). Therefore an unsteady computation of the whole turbulent flow domain is not conceivable in such a case.

### Outline of the present contribution

This is why we propose a three-step approach in the present study as sketched on Figure 2. The first step is the simulation of the source, the second is the propagation from the source to an intermediate distance, which would typically correspond to the limit of the turbulent flow around the vehicle in a practical situation and the third is the propagation into the far field in a medium at rest with or without ground effects. Since the distance from the source to the intermediate region between step 2 and step 3 is larger than the dominant wavelength and not very large compared to the train height, it corresponds to an acoustic far field and a geometric near field condition: therefore it will be referred to hereafter as “near-far-field”. For the first step, an existing LES database [9] describing a low Mach number flow past a

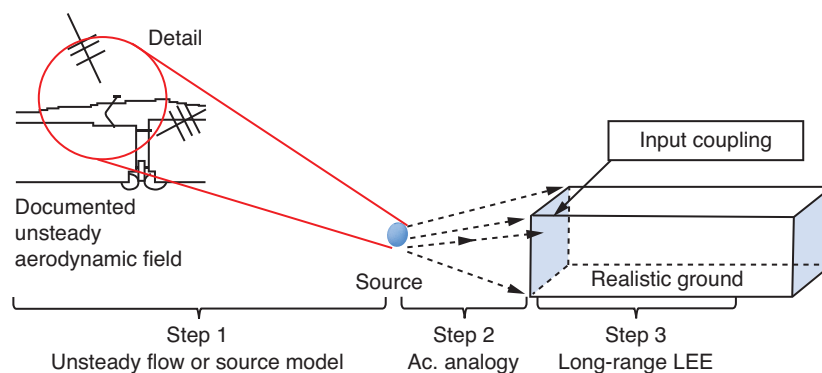


**Figure 2:** Sketch of the three-step approach.

circular cylinder is chosen as source flow field, the step 2 propagation is achieved using the Ffowcs Williams Hawkins (FWH) analogy in a free field at rest, whereas the step 3 propagation is predicted with the aforementioned LEE code. The flow past a cylinder is particularly relevant since pantographs are assemblies of bars that are variously oriented with respect to the surrounding flow. Although the pantograph elements are in general not circular but rather elliptic cylinders and despite the fact that the junctions between pantograph elements (*e.g.* the pantograph “knee”) are major noise contributors, the mechanisms of sound generation are physically similar to those involved in the circular cylinder flow. Moreover, the flow past a circular cylinder is well documented in the literature [10]-[19], which provides useful validation data for the simulation. Therefore it was considered as a representative test case in the present study. The main novelty with respect to prior work is the coupling between the FWH near-far-field output and the LEE input, as well as the application of the LEE code to non-academic sources. The long-term objective of this work is to provide a method where step 1 source models written in the time domain such as stochastic source models may replace the expensive LES used in the present article. Such models might be tested and tuned by comparison with the LES based computations shown hereafter.

In section 2, the LES approach as well as the database obtained for the cylinder case are described. The experimental validation against results from various references is shown and discussed in section 3. An example of the sound computations using the FWH analogy is also shown. In section 4, the long-range propagation code (step 3) is described whereas the coupling with the FWH output from step 2 is discussed in section 5, where results of the full approach are also shown.

## 2. THE LES DATABASE

### Test case and flow configuration

The test case is a  $M \sim 0.2$  flow past a circular cylinder whose diameter  $D$  is 10 mm and length (span) is 90 mm. The flow is initially laminar but due to the diameter based Reynolds number ( $Re \sim 84\,000$ ), the transition to turbulence of the shear layers detaching from the cylinder sides happens immediately after separation. As a result, the vortex shedding of the cylinder that occurs at a preferred frequency  $f_0$  corresponding to a Strouhal number  $St \sim 0.2$ , is strongly perturbed by the turbulent fluctuations and the spectra are characterised by broad peaks around the shedding frequency and its harmonics. This situation is described as subcritical [10], the critical point being the transition to turbulence of the cylinder boundary layers upstream of the separation point.

The purpose of the test case is to provide some reference data to assess and verify the coupling between the FWH sound computations and the long-range LEE code. Additionally to the validation against data from the literature, the LES data have been compared to dedicated flow and sound measurements. These were obtained in an anechoic wind tunnel on a  $30D = 300$  mm length (span) cylinder that was located in the potential core of a rectangular jet and mounted between two wooden plates [20].

## LES computations

A LES simulation has been carried out and validated against the experimental data as discussed in [9]. The code is a finite-volume solver named TurbFlow. It solves the filtered unsteady compressible Navier-Stokes equations:

$$\frac{\partial \bar{\rho}}{\partial t} + \frac{\partial \bar{\rho} \tilde{u}_j}{\partial x_j} = 0$$

$$\frac{\partial \bar{\rho} \tilde{u}_i}{\partial t} + \frac{\partial \bar{\rho} \tilde{u}_i \tilde{u}_j}{\partial x_j} = -\frac{\partial \bar{p}}{\partial x_i} + \frac{\partial}{\partial x_j} [(\bar{\mu} + \mu_{sgs}) \tilde{\sigma}_{ij}] \quad i = 1, 2, 3$$

$$\frac{\partial \bar{\rho} \tilde{e}_i}{\partial t} + \frac{\partial [(\bar{\rho} \tilde{e}_i + \bar{p}) \tilde{u}_j]}{\partial x_j} = \frac{\partial}{\partial x_j} [(\bar{\mu} + \mu_{sgs}) \tilde{\sigma}_{ij} \tilde{u}_i] + \frac{\partial}{\partial x_j} \left[ \left( \bar{\kappa} + \frac{\mu_{sgs} c_p}{Pr_{sgs}} \right) \frac{\partial \tilde{T}}{\partial x_j} \right]$$

where  $\sigma_{ij} = 2S_{ij} - \frac{2}{3}\delta_{ij} \frac{\partial u_k}{\partial x_k}$ , and  $S_{ij}$  is the strain rate tensor.

These equations predict the evolution of the largest turbulent eddies in the time domain, whereas the small scales at grid level remain unpredicted. The energy transfer between the large and the unresolved subgrid scales is modelled by a so-called subgrid scale model (SGS) as a diffusive process via the subgrid scale viscosity  $\mu_{sgs}$  and the subgrid scale Prandtl number  $Pr_{sgs} = \frac{\mu_{sgs} c_p}{\kappa}$ . In the classical Smagorinsky model,  $\mu_{sgs}$  is added to the molecular viscosity as a function of the strain rate tensor  $S_{ij}$ , the filtered density  $\bar{\rho}$ , the filter size  $\Delta$  and a model constant, the Smagorinsky constant  $C_S$ :

$$\mu_{sgs} = \bar{\rho} (C_S \Delta)^2 \sqrt{2 \widetilde{S_{ij} S_{ij}}}$$

In this model, the strain rate is directly computed from the instantaneous flow, leading to overestimates of the transfer in wall regions. In the present study, the Shear Improved Smagorinsky Model (SISM) developed by L ev eque *et al.*[21] is used. It is developed from the analysis of the turbulence budget and accounts explicitly for the influence of the mean shear  $\langle S \rangle$ :

$$\mu_{sgs} = \bar{\rho} (C_S \Delta)^2 \left( \left| \widetilde{S_{ij}(\mathbf{x}, t)} \right| - \left| \langle \widetilde{S_{ij}(\mathbf{x}, t)} \rangle \right| \right)$$

$\langle S \rangle$  is obtained by using an appropriate (Kalman) time filter for the running averaging process that remains local in space and time. It is one of the most recent time filters to be found in the literature in this context [22], [23], [24] and will not further be discussed here.

### Cylinder flow computation

The LES was carried out for a  $V_0 = 70 \text{ m}\cdot\text{s}^{-1}$  uniform flow past a  $D = 10 \text{ mm}$  diameter and  $L = 9D = 90 \text{ mm}$  long circular cylinder. The domain is also cylindrical with the same axis as the actual cylinder. It extends radially over  $20D$ . The mesh is refined in the wake of the cylinder in order to properly model the near wake. It is made of 9 M points. Near the walls the mesh size reduces to a few wall units in the radial, azimuthal and spanwise directions respectively:

$$\Delta r_{max}^+ \approx 1; r\Delta\theta_{max}^+ \approx 20; \Delta z_{max}^+ \approx 25$$

This corresponds to a well-resolved mesh according to criteria that apply to this type of simulations.

On the domain sides that limit the cylinder length, a periodicity condition is applied whereas Non Reflective Boundary Conditions are applied on the other boundaries. Since the LES is not the purpose of the present study, the validation of the unsteady flow that is discussed in chapter 3 of Cahuzac's PhD Thesis [9], will not be further discussed here. On Figure 4 a typical snapshot of the instantaneous flow is shown along with a view of the mesh in the vicinity of the cylinder. The coordinate system  $(O,x,y,z)$  for this configuration as well as the angles  $\varphi$  and  $\theta$  are illustrated on Figure 3.

### From source to near-far-field

The sound field is computed in the acoustic far field, that is, a few wavelengths away from the source ( $R > \lambda$ ). In the case of the cylinder, the distance ( $R \sim 1.85 \text{ m}$ ) is also in the geometric far field that is,  $R > D$  and  $R > L$ . As will be discussed in section 5 and was already mentioned in the introduction, for a train application the distance  $R$  will be chosen near the limit of the airflow surrounding the train, which will correspond to an acoustic far field but a geometrical near field with regard to the train height. The reason is that the long-range computation has to start where ground effects might play a role, not too far from the tracks.

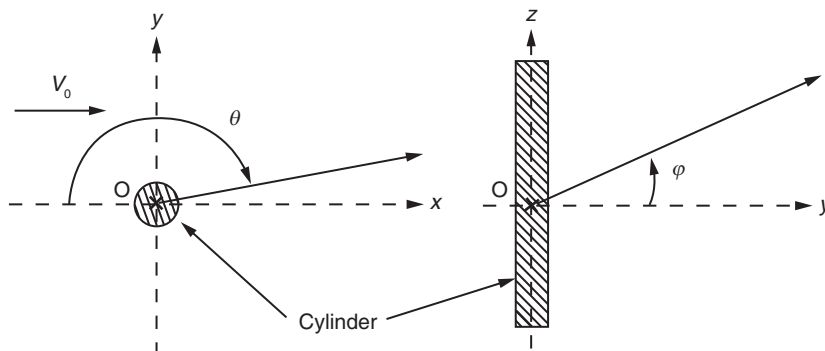


**Figure 3:** Coordinates of cylinder flow configuration

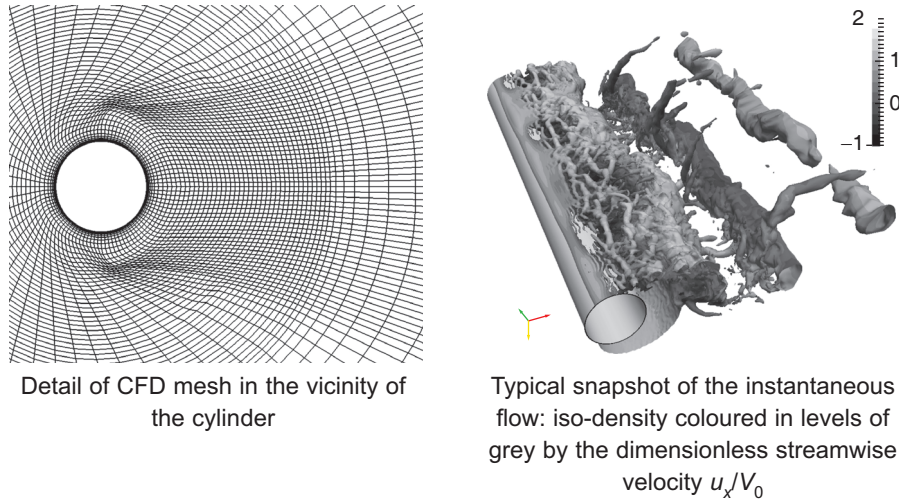


**Figure 4:** CFD mesh and instantaneous flow visualisation at  $V_0 = 70$  m/s.

This “near-far-field” computation is carried out by feeding the unsteady pressure field on the cylinder wall into the Ffowcs Williams and Hawkins (FWH) analogy discussed herein. The FWH analogy is an exact integral formulation of the momentum equation [25] based on a convolution of the flow equations by the free field Green’s function in a homogeneous medium that is either at rest or in uniform motion. This exact equation provides an expression of the pressure that approximates the actual sound pressure, provided some assumptions are made: in particular the flow effects onto propagation are assumed to be negligible. A computer-friendly version has been developed by Brentner and Farrasat [26] for both material and arbitrary control surfaces. Moreover, if the volume sources due to the direct radiation of flow eddies can be neglected (which is the case at low Mach numbers), the FWH formulation can be restricted to two surface integrals. Let the surfaces be defined by a map  $g(\mathbf{x}, t) = 0$ , whose outer normals are denoted by  $\mathbf{n}$ . The surface integrals write:

$$4\pi p' = -\frac{\partial}{\partial x_i} \iint_{g=0} \left[ \frac{L_i}{r(1-M_r)} \right]_{ret} ds + \frac{\partial}{\partial t} \iint_{g=0} \left[ \frac{Q}{r(1-M_r)} \right]_{ret} ds$$

The integrands are evaluated at the retarded time:

$$\tau_{ret} = t - \frac{|\mathbf{x} - \mathbf{y}(\tau_{ret})|}{c_0}$$

In these equations, the term:

$$L_i = \left( (p - p_0)\delta_{ij} - \tau_{ij} \right) n_j + \rho u_i (u_n - v_n)$$

denotes the  $i$ -th component of the unsteady surface momentum loading by the local fluctuating gage pressure ( $p - p_0$ ), the viscous stresses and the normal momentum flux  $\rho u_i(u_n - v_n)$ . The unsteady mass flux is:

$$Q = \rho_0 \left[ \left( 1 - \frac{\rho}{\rho_0} \right) v_i + \frac{\rho u_i}{\rho_0} \right] n_i$$

where  $u_i, v_i$  are the flow and surface velocity components respectively. This formulation is valid for an arbitrary control surface. When the surface is a hard wall, the normal velocity vanishes. If additionally, viscous stresses are neglected and the solid surface is not accelerated with respect to the steady flow, only the unsteady pressure term remains, which considerably simplifies the algebra. The expression of the loading term is rearranged to appear as a time derivative at the emission time:

$$-\frac{\partial}{\partial x_i} \iint_{s=0} \left[ \frac{L_i}{r(1-M_r)} \right]_{ret} ds = \iint_{s=0} \left[ \frac{1}{(1-M_r)} \frac{1}{c_0} \frac{\partial}{\partial \tau} \left( \frac{L_i r_i}{r(1-M_r)} \right) + \frac{L_i r_i}{r^2(1-M_r)} \right]_{ret} ds$$

In the present study, this form of the Ffowcs Williams and Hawkings analogy is applied to the unsteady surface pressure field that is directly predicted by the LES.

### 3. RESULTS

The results for the flow computation past a cylinder are summarised hereafter where they are compared to various experimental data from the literature that are obtained in the same flow regime.

#### Global parameters

First global aerodynamic parameters are considered, the mean and the root mean square (rms) drag coefficients, the rms lift coefficient, the mean separation angle  $\theta_s$  ( $\theta = 0^\circ$  corresponds to the upstream stagnation point), the mean length of the recirculation bubble and the Strouhal number of the shedding frequency.

The values are listed in Table 1 for the present computation along with the corresponding range of values found in the literature. It can be seen that most LES results lie within the range of their experimental values, some being slightly out of the

**Table 1: Lift and drag coefficients, shedding frequency, separation angle and recirculation bubble length of the present LES and of various experiments.**

	LES	Experimental results
$\bar{C}_D$	1.20	[1.0 – 1.35]
$C'_D$	0.048	[0.05 – 0.16]
$C'_L$	0.511	[0.4 – 0.8]
St	0.2	[0.18 – 0.2]
$\theta_s$	86°	[83 – 84]
$l_r$	1.21D	1.25 D

range (by a few *per cent*): the separation angle and the recirculation length that are physically linked to each other.

### Pressure distributions and velocity profiles

On Figure 5, the pressure coefficient  $C_p$  and its rms value  $C_p'$ , as well as the friction coefficient  $C_f$  are plotted along the circumference of the cylinder for the present computation. They are compared to the corresponding mid-span quantities from several references [11], [12], [13], [15], [17], [18] and [19].

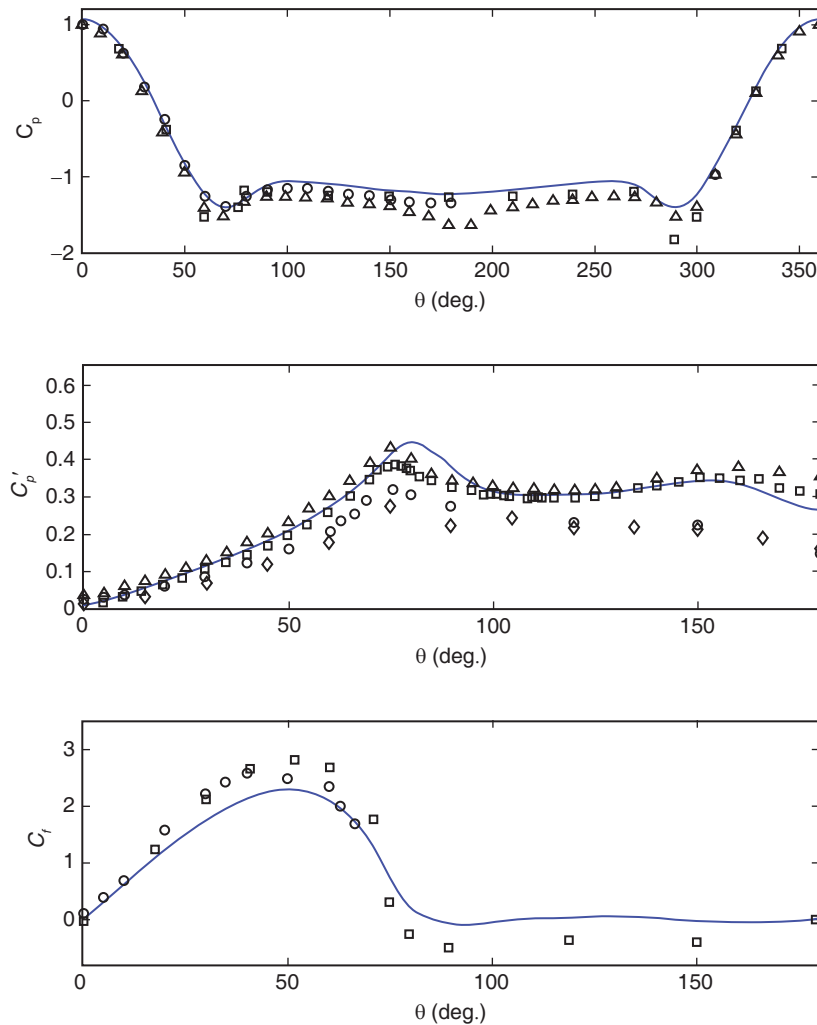


**Figure 5:** Mean and rms pressure coefficients, mean friction coefficient. — present computation; symbols: results from [11], [12], [13], [15], [17], [18] and [19].

The mean pressure coefficient is remarkably well predicted given the dispersion of the experimental data. The inflection point of the pressure coefficient at about  $80\text{-}90^\circ$  characterises the release of the adverse pressure gradient due to the flow separation, which is also well predicted as shown in Table 1. This quantity is important for the sound prediction as it is directly linked to the shedding frequency. For the rms pressure coefficient, the computation also compares favourably to the experimental data if one considers the experimental dispersion. This is important for the sound prediction issue, as the rms value is representative of the cylinder surface pressure fluctuations. For the friction coefficient, the computation does not fit extraordinarily well to the measured data.

The mean and rms velocity profiles (the mean modulus and its rms value) are plotted at two flow cross-sections on Figure 6, one at the cylinder side slightly downstream of the centre ( $x/D = 0.1$ ) and the other downstream of the cylinder in its near wake, 1.3 diameters from the cylinder wall ( $x/D = 1.8$ ). The results are compared to experimental data as reported by Cahuzac [9]. At  $x/D = 0.1$  the agreement is excellent. In the near wake ( $x/D = 1.8$ ), the wake width is very well predicted but the computation underestimates the wake depth and overestimates the wake turbulence. Since the measurements are carried out in the near wake where the instantaneous flow direction might be reverse intermittently, it is likely that the hot-wire fails to provide an accurate average of the fluctuations and that

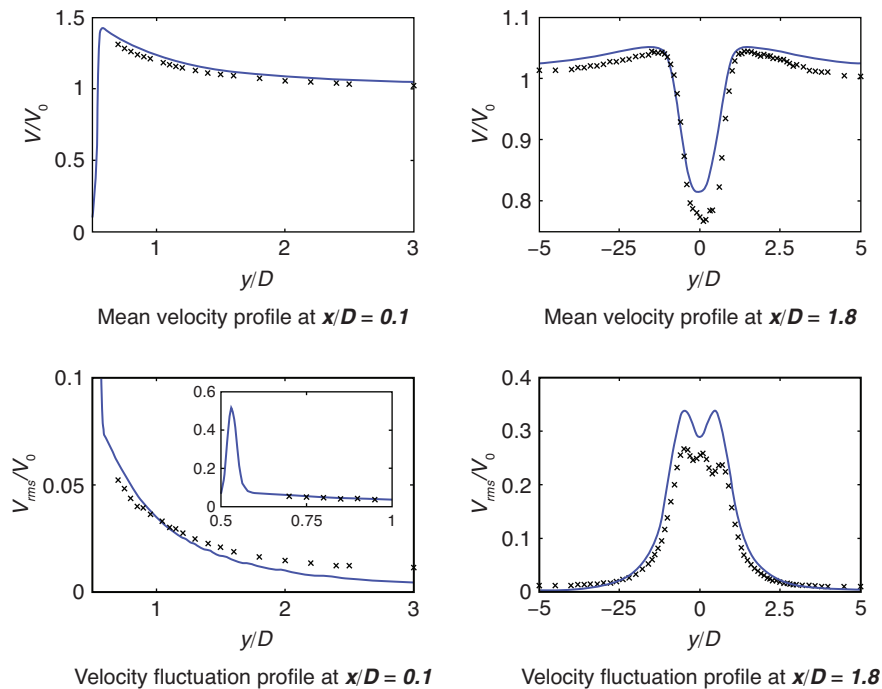


**Figure 6:** Velocity profiles aside the cylinder and in the near wake: — present computation; symbols: Hot wire results from [9].

the actual wake is not as deep as suggested by the hot wire data. Therefore it is difficult to conclude about the numerical accuracy in this region.

Nevertheless, despite this discrepancy, the overall agreement between the LES mean flow data and experimental results from the literature is very good and gives some confidence in the numerical results.

### Unsteady flow

The spectrum of the velocity fluctuations in the upper shear layer ( $y/D = 0.6$ ) of the near wake ( $x/D = 1.8$ ) is plotted on Figure 7. In this region the main shedding frequency ( $f_0$ ) and its even harmonics  $(2m + 1)f_0$  are stronger than in the centre of the wake where the influence from both shear layers is felt. This is confirmed by the results shown here: the second harmonic ( $3f_0$ ) can be seen on the LES spectrum. However the peaks due to the vortex shedding are overestimated by the LES (or underestimated by the hotwire), which is consistent with the conclusions drawn about Figure 6 (bottom right plot). The broadband part of the experimental spectrum is remarkably well predicted up to the first harmonic ( $2f_0$ ). Beyond this frequency, the experimental spectrum decays faster than the LES one. It should be noted that the high frequency part of the LES spectrum tends to a  $-5/3$  power slope, which gives some consistency to the numerical result although the turbulence is still highly dominated by the large intermittent vortices at this location.

### Near-far field

The FWH analogy is applied to the LES dataset for a receiver located almost normal to the flow at  $R = 1.85$  m from the cylinder centre ( $\theta = 94^\circ$ , that is  $4^\circ$  into the downstream direction). In order to compare the numerical results with the microphone measurements that were obtained from a much longer cylinder ( $L_{exp} = 30D$ ), the former are extrapolated with a correction proposed by Kato [27]: the correction to be added to the Power Spectral Density (PSD) of the simulation reads:  $10 \log(L_{exp}/L)$ ,  $L$  being the

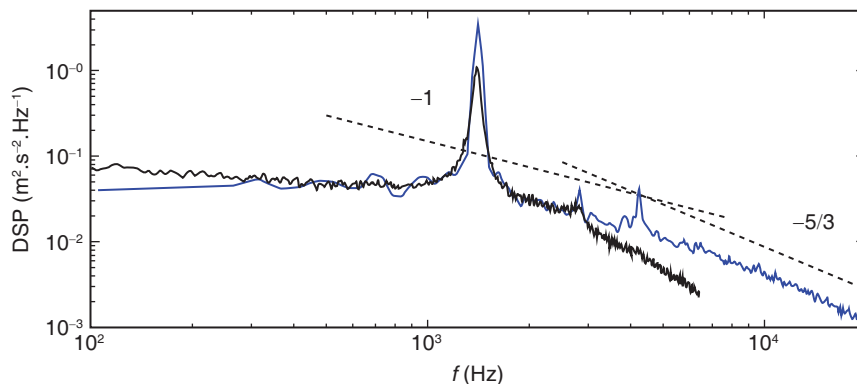


**Figure 7:** Velocity spectrum in the upper shear layer ( $y/D = 0.6$ ) of the near wake ( $x/D = 1.8$ ): — present computation; — Hot wire results from [9].

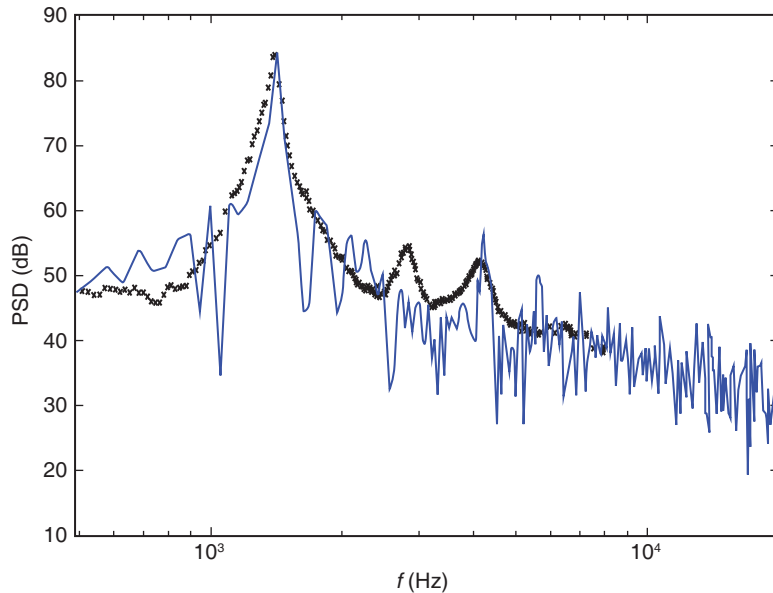


**Figure 8:** Sound spectra at  $R = 1.85$  m and  $\theta = 94^\circ$ . — present computation; black symbols: microphone measurement from [9].

length of the cylinder in the simulation. Shear layer refraction is negligible for this receiver position. The spectra are shown on Figure 8.

The main peak and its broadening about the shedding frequency are well captured. The high frequency tail of the spectrum is also well predicted. The low frequency part ( $< 500$  Hz) is not represented since the physical time covered by the simulation is too short to give accurate results in the low frequency range, and its experimental counterpart is dominated by installation effects (jet noise etc.). Beside the fact that the first harmonic frequency ( $2f_0$ ) due to the fluctuating drag is not captured by the computations, the agreement is very good over the whole frequency range.

All these results show that the LES for the cylinder contains high quality data even though some results are not perfect. Therefore it will be used hereafter to validate the coupling with the long-range LEE (step 3). Before this final step, the LEE code will be described in the next section.

#### 4. LONG RANGE LEE COMPUTATIONS

The long-range propagation tool uses finite-difference time-domain methods to solve the Linearised Euler Equations (LEE). The solver has been developed by Cotté [28] and Dagna [5]. It enables to account for most of the physical phenomena that play a role on outdoor sound propagation.

- It accounts for ground effects through a time-domain impedance boundary condition.
- The ground topography is also modelled.
- Meteorological effects can also be included. Wind speed and temperature profiles are readily taken into account without the effective sound speed approximation.

For these reasons, time-domain simulations are better suited than FWH-type aeroacoustic analogies since they don't require appropriate Green functions that exist only for simple cases.

This propagation tool has been applied in the European Program *Acoutrain* [29] to provide reference values for a variety of basic test cases in order to validate a global source-to-far field tool. The LEE and the boundary conditions used in the solver are briefly summarised hereafter.

### Linearised Euler Equations (LEE)

The Linearised Euler Equations are obtained by linearising the fluid mechanics equations around mean flow values. Denoting the mean flow velocity by  $\mathbf{V}_0$  and the mean air density by  $\rho_0$ , the acoustic pressure  $p$  and velocity  $\mathbf{v}$  are governed by:

$$\frac{\partial p}{\partial t} + \mathbf{V}_0 \cdot \nabla p + \rho_0 c_0^2 \nabla \cdot \mathbf{V}_0 = \rho_0 c_0^2 q$$

$$\rho_0 \frac{\partial \mathbf{v}}{\partial t} + \rho_0 (\mathbf{V}_0 \cdot \nabla) \mathbf{v} + \rho_0 (\mathbf{v} \cdot \nabla) \mathbf{V}_0 + \nabla p = \mathbf{F}$$

In the above equations, the terms  $q$  and  $\mathbf{F}$  correspond to mass sources and to external forces. These equations are valid up to the order  $|\mathbf{V}_0|^2/c_0^2$ . The Linearised Euler Equations are solved using high-order finite-difference time domain techniques developed in the aeroacoustics team in Ecole Centrale de Lyon [30], [31], [32]. To account for the topography, curvilinear coordinates are used. However, in the present context of validation, we will focus only on propagation above a flat ground and most examples will be in free space in order to allow straightforward comparisons with the free space integral formulation.

### Boundary conditions (BC)

#### *Non-reflective boundary conditions*

At the outer boundaries, the radiation conditions proposed by Tam & Dong [33] are used. They are based on an asymptotic expansion of the LEE. Unlike the well-spread approach of perfectly matched layers, these boundary conditions require the approximate position of the source region as input data. In the free-field cylinder computations, the position of the source region is set to the centre of the cylinder. In the case of a ground surface, an image source region exists, and its position is symmetric to that of the source region relative to the ground surface. In that case, the origin for the

computation of the boundary conditions is set at the ground surface between the source region and the image source region.

#### *Time domain impedance boundary conditions*

The reflection on the ground surface has to be taken into account to have realistic estimates of sound pressure levels in outdoor sound propagation studies. However, some difficulties are encountered when translating the impedance boundary condition into the time-domain.

As known from textbooks or recalled in [34], the impedance boundary condition for a locally-reacting ground surface writes in the frequency-domain as  $\hat{p}(\omega) + \hat{Z}(\omega)\hat{v}_n(\omega) = 0$ , where  $\omega$  is the angular frequency,  $\hat{Z}(\omega)$  is the surface impedance,  $\hat{p}(\omega)$  and  $\hat{v}_n(\omega)$  are the Fourier transforms of the pressure and the acoustic velocity normal to the ground. The normal is pointing out of the ground into the domain. In the time domain, the impedance boundary condition reads:

$$p(t) = -\int_{-\infty}^t Z(t-t')v_n(t')dt'$$

where  $Z(t)$  is the inverse Fourier transform of the surface impedance.  $\hat{Z}(\omega)$  is classically given in the literature only for positive frequencies. In order to define  $Z(t)$ ,  $\hat{Z}(\omega)$  must be extended to the entire complex plane [35]. Moreover, not all surface impedance models are physically admissible. Three necessary conditions are proposed in [35]: (i)  $Z(t)$  must be causal, (ii)  $Z(t)$  must be real, and (iii)  $\text{Re}[\hat{Z}(\omega)] > 0$  for  $\omega > 0$  because the ground absorbs energy. These conditions have been checked for some popular impedance models in the outdoor sound propagation community in [36].

In the present study, a Time Domain Boundary Condition (TDBC) derived by Reymen *et al.* [37] on the basis of work done in electromagnetism [38] has been implemented into the LEE solver. This TDBC has been introduced in the outdoor sound propagation community by Cotté *et al.* [39]. It is based on an approximation of the impedance in the frequency-domain by a rational function:

$$\hat{Z}(\omega) \approx Z_\infty + \sum_{k=1}^N \frac{A_k}{\lambda_k - i\omega}$$

For this rational function, the causality condition is verified if and only if the real parts of the poles  $\lambda_k$  are positive [37]. The absorption condition  $\text{Re}[\hat{Z}(\omega)] > 0$  for  $\omega > 0$ , must be verified by each set of coefficients  $(A_k, \lambda_k)$ .

Since the inverse Fourier transform of the impedance defined by the rational function, that is,

$$Z(t) = Z_\infty \delta(t) + \sum_{k=1}^N A_k e^{-\lambda_k t} H(t),$$

must be real valued (see *e.g.* [35]), the poles  $\lambda_k$  are real or complex conjugates. For the sake of simplicity, we only present the TDBC for real poles. However, complex

conjugate poles can also be taken into account [37]. Various methods are discussed in [39] to determine the coefficients  $\lambda_k$  and  $A_k$ . Let us denote by  $p^{(m)}$  and  $v_n^{(m)}$  the values of pressure and acoustic velocity normal to the ground at the discretized time  $m\Delta t$ . By introducing the expression of the time dependent impedance given by the previous expression of  $Z(t)$  in the convolution integral, a recursive convolution method is used. Assuming that the normal velocity is constant over a time step, the following relation between  $p^{(m)}$  and  $v_n^{(m)}$  is obtained:

$$p^{(m)} = -Z_\infty v_n^{(m)} + \sum_{k=1}^N A_k \phi_k^{(m)}$$

where  $\phi_k^{(m)}$  are called the accumulators. They are given by the recursive expression:

$$\phi_k^{(m)} = -v_n^{(m)} \frac{1 - e^{-\lambda_k \Delta t}}{\lambda_k} + \phi_k^{(m-1)} e^{-\lambda_k \Delta t}$$

Details about the derivation of the last two equations can be found in [37]. These TDBC's have been validated on several test cases [5], [6] and have also been extended to account for non-flat ground surfaces [6].

## 5. COUPLING FWH WITH LEE

### Coupling technique

The sound field computed with the FWH analogy using the free space Green's function, from the source to the "near-far-field", is coupled to the long-range propagation tool along the inlet boundary of the long-range computational domain. The coupling is carried out in a region where two assumptions about the waves and the surrounding medium can be made. The first assumption is that the distance from the source to the coupling region is long enough to ensure the acoustic far field condition, that is, the distance is at least about a wavelength or more. As a result the waves can be locally approximated by plane waves thus providing very simple relations between the inlet variables (pressure and velocity):

$$u'_y = \frac{p'}{\rho_0 c_0} \cos(\varphi)$$

$$u'_z = \frac{p'}{\rho_0 c_0} \sin(\varphi)$$

for the two velocity components ( $y$  horizontally away from the train,  $z$  vertically away from the ground and  $\varphi$  the angle of the current point at the inlet boundary with respect to  $y$ ).

The other important assumption is that the coupling region is not too far from the source, in order for the ground effects not to be significant in the first part of the computation. Typically, the coupling region could be the limit of the flow region surrounding the train or the limit of the track surface where the ballast starts to slope down.

Finally, a last technical adjustment had to be made in the LEE computation: the FWH computation is indeed carried out in a uniform flow. Therefore, in the case of a stationary source with a stationary observer, it assumes a uniform reverse flow, which is not the case in the long-range propagation domain. The validation of the coupling approach is based on a comparison with the direct FWH computation between the source and the far-field. As a result, a correction has to be applied to the speed of sound in order to compensate this effect. Note that this comparison is only possible because the source is located in free space. Since the mean velocity is normal to the LEE domain in our applications, the correction simply writes:  $c_{eq} = \sqrt{c_0^2 - V_0^2}$ .

## Results for long-range computations of the cylinder radiation

### *Validation on the Cylinder flow in free space*

First, the coupling methodology is applied to a 2-D propagation domain in free field as sketched in Figure 9. The validation on the LES test case is based on a double approach: each approach starts from the LES cylinder surface pressure. One considers free field propagation that is required for both approaches to be valid. In the first approach the long-range far field is directly computed with FWH at three observer locations ( $y = 5, 7$  and  $10$  m). In the second approach, the three-step method is applied: the FWH analogy propagates the sound to the long-range domain inlet, that is the “near-far-field”, where it is coupled to the long-range LEE computation and then propagated up to the same observer positions as the direct approach. Since the starting points and the receiver locations are the same and the FWH algorithm has been validated elsewhere [40], the comparison of the two approaches evaluates the quality of the coupling.

For the long-range computation, following boundary conditions are applied to the CAA-domain. As stated above, the acoustic field computed from the FWH analogy is imposed at the left boundary. At the other boundaries, the radiation boundary condition of Tam and Dong [33] is applied.

In the FWH computation, the cylinder is moving at constant speed  $V_0$  along  $x$ -direction in a medium at rest whose sound speed is  $c_0$ . A line of receivers is initially located at  $x = 0$  m,  $y = 3$  m and from  $z = -1.25$  m to  $z = 1.25$  m. It is also moving in the  $x$ -direction at speed  $V_0$ . This problem is equivalent to a stationary cylinder and

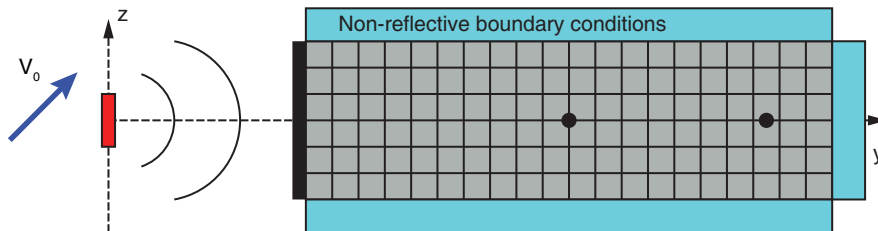


**Figure 9:** Sketch of the validation test case.

stationary receivers in a moving medium at speed  $-V_0$ . In the LEE solver, the sound propagation is only computed in the plane  $x = 0$  that is normal to  $V_0$ . In that case, the sound speed does not correspond to  $c_0$ , but to the equivalent sound speed  $c_{eq} = \sqrt{c_0^2 - V_0^2}$  already mentioned in the previous section.

Note also that in the present case, the LEE computation is carried out in a 2-D domain. Therefore a correction is applied to account for spherical spreading. If  $y_{ref}$  and  $y$  denote respectively the  $y$ -position of the inlet boundary and that of the receiver relative to the source, the pressure is multiplied by the correction factor  $\sqrt{y_{ref}/y}$ .

Results are shown in Figure 10 as time series: the agreement is almost perfect, except for a little oscillation at the beginning and the end of the signal. The transient lasts for about one shedding period and its amplitude is an order of magnitude below the signal.

In order to quantify the qualitative agreement observed on Figure 10, spectra are computed from these signals and plotted in Figure 11 for two receivers at  $y = 5$  m and 10 m. The overall agreement is excellent up to 2500 Hz. In particular, the broad peak at the main shedding frequency is very well reproduced by the long-range computation. Above this frequency the spectrum obtained from the long-range simulation falls off rapidly. This is due to the grid size that is too coarse for the higher frequencies. It can also be

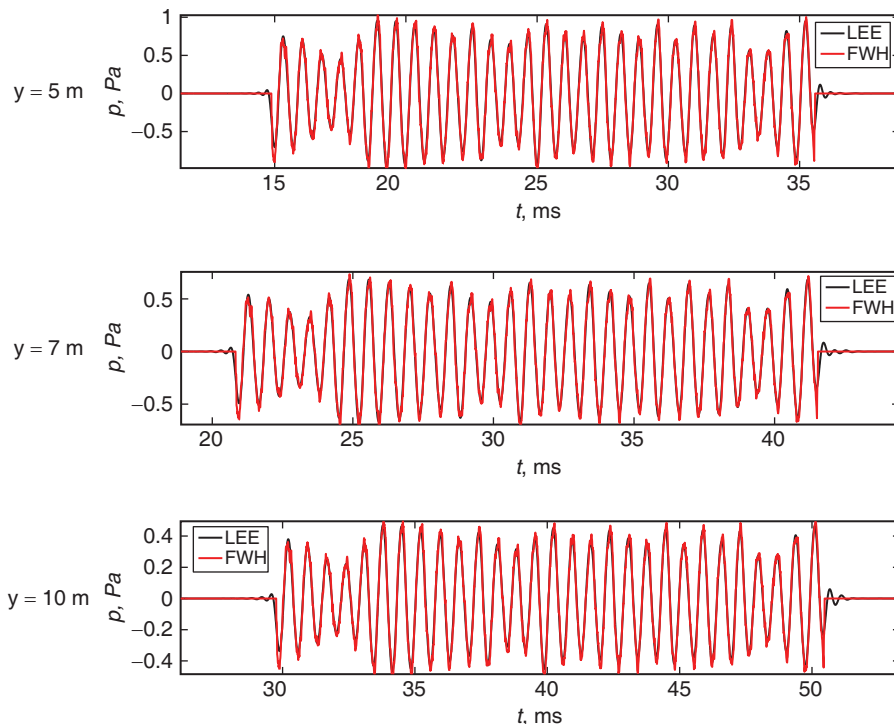


**Figure 10:** Comparison of the far fields obtained via the two prediction methods. Direct approach (FWH only) : — FWH; coupled approach (FWH) and (LEE): — LEE.

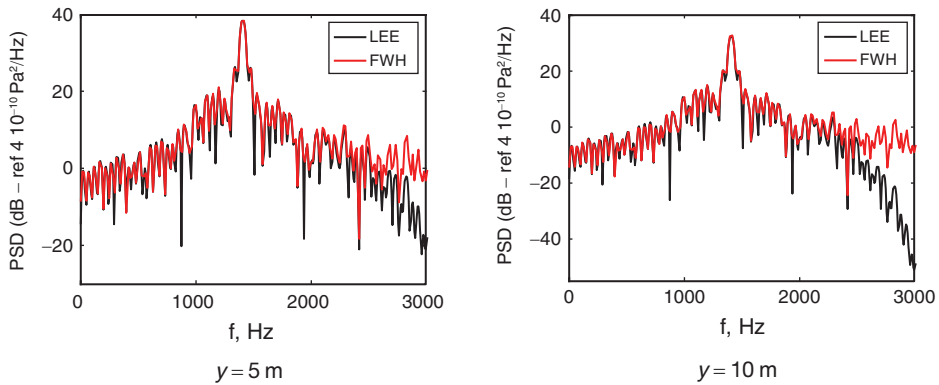


**Figure 11:** Sound spectra at two far field receivers obtained by the two approaches. Direct approach (FWH only) : — FWH ; coupled approach (FWH and LEE): — LEE.

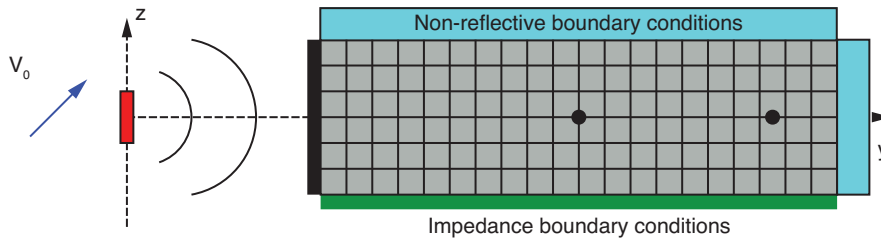


**Figure 12:** Propagation of acoustic waves emitted by the cylinder above an impedance ground surface.

observed that all the spectra are quite wiggly, which is due to the shortness of the available LES time series.

Thus it can be concluded that the coupling between the long-range computation and the FWH output works perfectly well. It should be noted that it justifies *a posteriori* the local plane wave approximation made at the inlet boundary and validates the velocity correction.

#### *Computations with various ground impedances*

In this subsection, we demonstrate the potential of this source-to-far-field prediction tool, by testing the algorithm for flat grounds with two different ground impedances:

- a rigid ground surface
- a grassy ground surface using Miki's impedance model [1], with an air flow resistivity and a layer thickness equal respectively to  $140 \text{ kPa}\cdot\text{s}\cdot\text{m}^{-2}$  and  $0.018 \text{ m}$ .

The configuration is sketched on Figure 12. The numerical domain is the same as the one used in the previous subsection. The impedance boundary conditions that are briefly described in Section 4 are applied to the ground surface.

Snapshots of the acoustic pressure are represented in Figure 13. It can be seen that compared to free field conditions, the presence of a reflective boundary introduces

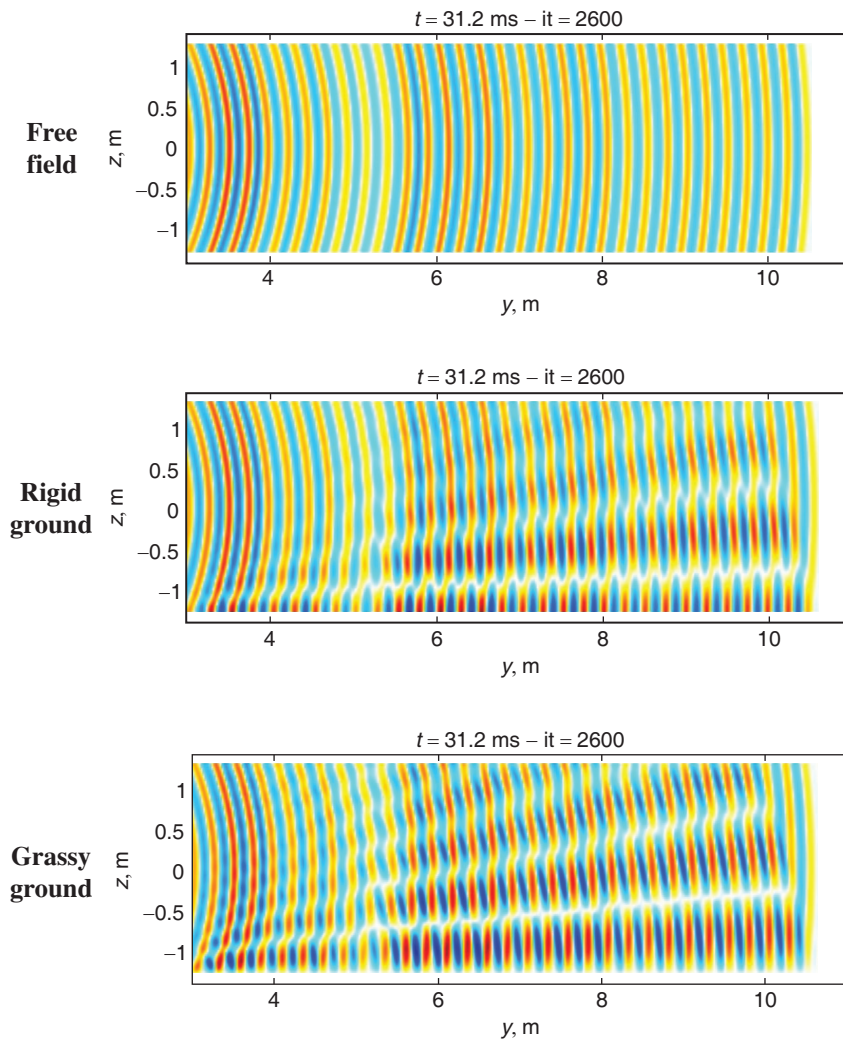


**Figure 13:** Snapshots of the acoustic pressure for free-field condition, rigid ground and grassy ground.

interference patterns. Note also that the acoustic pressure field obtained with a finite-impedance ground surface is very different to that obtained with a rigid ground.

Figure 14 shows the evolution of the sound pressure level against  $z$  at  $y = 7$  m for the different cases. In free-field condition, the sound pressure level is almost constant, as it can be expected since the propagation is weakly directive and the distance to the source does not vary significantly along the vertical line. In the presence of a reflective ground, the constructive and destructive interference patterns (nodes and antinodes) already

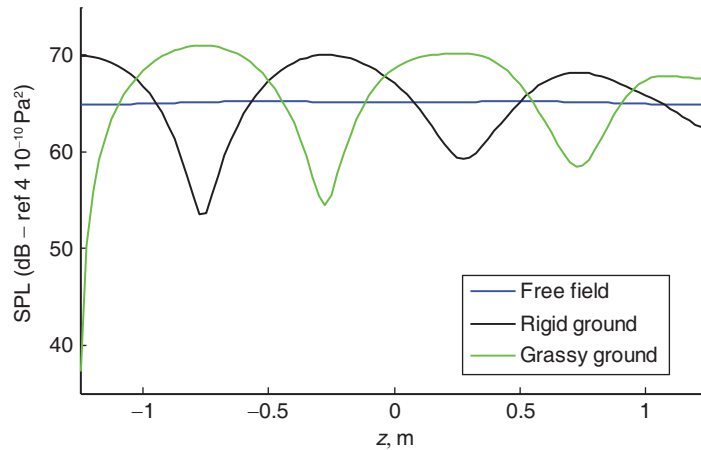


**Figure 14:** Sound pressure level versus  $z$  at  $y = 7$  m for different boundary conditions.

observed in Figure 13, are clearly visible, and their locations depend strongly on the boundary condition. Note also that the sound pressure level decreases significantly near the ground surface for a grassy ground.

These computations illustrate but a few possibilities of the LEE code. Other applications with a non-plane ground topography, including other materials such as ballast may be considered. For such materials, impedance models in the time domain have been developed and validated elsewhere for academic sources. Although such boundary conditions might also be applied here, this hasn't been done in the present study since no validation experiments are available so far.

## 6. CONCLUSIONS

The methodology discussed in the present article allows computing the sound radiated by an aerodynamic source far away into complex environments with non-flat topography and sound absorbing surfaces. It is based on a coupling between an acoustic analogy and a Linearised Euler Equation code. The acoustic analogy propagates the sound from the source to a region that lies already in the acoustic far field but is still in the geometric near field of the vehicle. The Linearised Euler Equation code propagates the sound away at large distances and is able to take into account complex ground reflexion conditions. The methodology has been successfully validated for the configuration of a flow past a cylinder in free space, where it could be compared to a free space Green function based analogy applied to a LES database. The comparison based on the same flow data showed almost perfect agreement up to the cut-off frequency of the mesh used for the long-range computation. However the methodology can also be adapted to any simplified source model that provides time-dependent aerodynamic fields such as stochastic noise generation models.

The methodology was finally applied to a half space limited either by a rigid ground or by a grassy ground. This was done to demonstrate the high potential of the approach discussed in this article. Other more complex applications might be considered in future work, given that some validation data were available. Unfortunately, passing-by measurements of train or aircraft noise (on the runway) do not provide information for a single source, which makes them not suitable for validation. Therefore dedicated wind tunnel experiments should be designed.

## ACKNOWLEDGEMENTS

This work has been funded by the European Community as part of the 7<sup>th</sup> Framework Project ACOURTRAIN n° FP7 - 284877. This work was conducted in the framework of the LabEx CeLyA (“Centre Lyonnais d’Acoustique”) of Université de Lyon, operated by the French National Research Agency (ANR-10-LABX-0060/ANR-11-IDEX-0007). The authors also wish to thank Dr E. Lévêque for his contribution to the LES computation.

## REFERENCES

- [1] Miki, Y., Acoustical properties of porous materials - Modifications of Delany-Bazley models, *J. Acoust. Soc. Jpn.*, **11(1)**, pp. 19–24. (1990).
- [2] Bérengier, M., Stinson, M.R., Daigle, G. A., Hamet, J. F., Porous road pavement: Acoustical characterization and propagation effects, *J. Acoust. Soc. Am.*, **101(1)**, pp. 155–162. (1997).
- [3] Cotté, B., Blanc-Benon, P., Poisson, F., Time-domain simulations of sound propagation in a stratified atmosphere over an impedance ground, *J. Acoust. Soc. Am.*, **125(5)**, EL202–207. (2009).
- [4] Dragna, D., Cotté, B., Blanc-Benon, P., Poisson, F., Time-domain simulations of outdoor sound propagation with suitable impedance boundary conditions, *AIAA J.*, **49**, pp. 1420–1428. (2011).
- [5] Dragna, D., Blanc-Benon, P., Poisson, F., Time-domain solver in curvilinear coordinates for outdoor sound propagation over complex terrain, *J. Acoust. Soc. Am.*, **133(6)**, pp. 3751–3763. (2013).
- [6] Dragna, D., Blanc-Benon, P., Poisson, F., Impulse propagation over a complex site: A comparison of experimental results and numerical predictions, *J. Acoust. Soc. Am.*, **135(3)**, pp. 1096–1105. (2014).
- [7] Dragna, D., Blanc-Benon, P., Poisson, F., Modeling of broadband moving sources for time-domain simulations of outdoor sound propagation, to appear in *AIAA J.* (2014).
- [8] Marsden, O., Bogey, C., Bailly, C., A study of infrasound propagation based on high-order finite difference solutions of the Navier-Stokes equations, *J. Acoust. Soc. Am.*, **135(3)**, pp. 1083–1095. (2014).
- [9] Cahuzac, A., *Aspects Cinétiques et acoustiques en simulation numérique des grandes échelles, application à l’étude du contrôle de l’écoulement de jeu en turbomachines*, Thèse de Doctorat, N°2012-17, Ecole Centrale de Lyon. (2012).

- [10] Zdravkovich, M. M., *Flow around circular cylinders, vol 1: fundamentals*, Oxford Science Publications, Oxford University Press, Oxford. (1997).
- [11] Achenbach, E., Distribution of local pressure and skin friction around a circular cylinder in cross-flow up to  $Re = 5 \times 10^6$ , *J. Fluid Mech.*, **34**, pp.625–639. (1968).
- [12] Anderson, E. A., Szewczyk, A. A., Effects of a splitter plate on the near wake of a circular cylinder in 2 and 3-dimensional flow configurations, *Exp. Fluids*, **23(161)**. (1997).
- [13] Batham, J. P., Pressure distributions on circular cylinders at critical Reynolds numbers, *J. Fluid Mech.*, **57(209)**. (1973).
- [14] B. Cantwell, B., Coles, D., An experimental study of entrainment and transport in the turbulent near wake of a circular cylinder, *J. Fluid Mech.*, **136**, pp. 321–374. (1983).
- [15] Szepessy, S., Bearman, P. W., Aspect ratio and end plate effects on vortex shedding from a circular cylinder, *J. Fluid Mech.*, **234**, pp. 191–217. (1992).
- [16] Gerrard, J. H., An experimental investigation of the oscillating lift and drag of a circular cylinder shedding turbulent vortices, *J. Fluid Mech.*, **11**, pp. 244–256. (1961).
- [17] Nishimura, H., Taniike, Y., Aerodynamic characteristics of fluctuating forces on a circular cylinder, *J. Wind Eng. Ind. Aerodyn.*, **89**, pp. 713–723. (2001).
- [18] Norberg, C., Fluctuating lift on a circular cylinder : review and new measurements, *J. Fluids Struct.*, **17**, pp. 57–96. (2003).
- [19] Yokuda, S., Ramaprian, B. R., The dynamics of flow around a cylinder at subcritical reynolds numbers, *Phys. Fluids A*, **2(5)**, pp. 784–791. (1990).
- [20] Jacob, M.C., Boudet, J., Casalino, D., Michard, M., A rod-airfoil experiment as a benchmark for broadband noise modelling, *Theoret. Comput. Fluid Dynamics*, **19(3)**, pp. 171–196. (2005).
- [21] L ev eque, E., Toschi, F., Shao, L., Bertoglio, J.-P., Shear-improved Smagorinsky model for large-eddy simulation of wall-bounded turbulent flows, *J. Fluid Mech.*, **570**, pp. 491–502. (2007).
- [22] Cahuzac A., Boudet J., L ev eque A., Borgnat P., Smoothing algorithms for mean-flow extraction in large-eddy simulation of complex turbulent flows, *Phys. Fluids*, **22(1)**, 125104. (2010).
- [23] Brockwell, P.J., Davies, R.A., *Time series: theory and methods*, Springer Series in Statistics, Springer, 2nd edition. (1991).
- [24] Harvey, A., *Forecasting, structural time series model and the Kalman filter*, Cambridge University Press. (1989).
- [25] Ffowcs Williams, J. E., Hawkings, D. L., Sound generation by turbulence and surfaces in arbitrary motion, *Phil. Trans. Roy. Soc.*, A264(1151), pp. 321–342. (1969).
- [26] Brentner, K.S., Farassat, F., Analytical comparison of acoustic analogy and Kirchhoff formulation for moving surfaces, *AIAA J.*, **36(8)**, pp. 1379–1386. (1998).
- [27] Kato, C., Iida, A., Takano, Y., Fujita, H., Ikegawa, M., Numerical prediction of aerodynamic noise radiated from low mach turbulent wake, *AIAA Paper 1993-0145*. (1993).

- [28] Cotté, B., *Propagation acoustique en milieu extérieur complexe : problèmes spécifiques au ferroviaire dans le contexte des trains à grande vitesse*, Thèse de Doctorat, Ecole Centrale Lyon, N° 2008–19. (2008).
- [29] Jacob, M. C., Aerodynamic sound generation model for a pantograph, *Deliverable ACOUTRAIN\_D3.8\_ECL\_2013\_02\_07*. (2013).
- [30] Bogey, C., Bailly, C., A family of low dispersive and low dissipative explicit schemes for flow and noise computations, *J. Comput. Phys.*, **194**, pp. 194–214. (2004).
- [31] Bogey C., de Cacqueray N., Bailly C., A shock-capturing methodology based on adaptative spatial filtering for high-order non-linear computations, *J. Comp. Phys.* **228**(5), pp. 1447–1465. (2009).
- [32] Berland J., Bogey C., Bailly C., Low-dissipation and low-dispersion fourth-order Runge-Kutta algorithm, *Comput. and Fluids*, **35** pp. 1459–1463. (2006).
- [33] Tam, C. K. W., Dong, Z., Radiation and outflow boundary conditions for direct computation of acoustic and flow disturbances in a non-uniform mean flow, *J. Comp. Acoust.*, **4**, pp. 175–201. (1996).
- [34] Attenborough, K., Sound propagation close to the ground, *Annu. Rev. Fluid. Mech.*, **34**, pp. 51–82. (2002).
- [35] Rienstra, S. W., Impedance models in time domain including the extended Helmholtz resonator model, *12<sup>th</sup> AIAA/CEAS Aeroacoustics Conference*, Cambridge, MA, USA, *AIAA Paper* 2006–2686. (2006).
- [36] Dragna, D., Blanc-Benon, P., Physically admissible impedance models for time-domain computations of outdoor sound propagation, *Acta Acust. united Ac.*, **100**(3), pp. 401–410. (2014).
- [37] Reymen, Y., Baelmans, M., Desmet, W. Time-domain impedance formulation based on recursive convolution, *12<sup>th</sup> AIAA/CEAS Aeroacoustics Conference*, Cambridge, MA, USA, *AIAA Paper* 2006–2685. (2006).
- [38] Luebbers, R. J. and Hunsberger, F., FDTD for Nth-order dispersive media, *IEEE Trans. Antennas Propag.*, **40**, pp. 1297–1301. (1992).
- [39] Cotté, B., Blanc-Benon, P., Bogey, C., Poisson, F., Time-domain impedance boundary conditions for simulations of outdoor sound propagation, *AIAA J.*, **47**(10), pp. 2391–2403. (2009).
- [40] Casalino, D., An advanced time approach for acoustic analogy predictions, *J. Sound Vib.*, **261**, pp. 583–612. (2003).